Vacancy clustering effect on the electronic and transport properties of bilayer graphene nanoribbons

Reference:
Miranda Lucas, da Costa Diego Rabelo, Peeters François, Costa Filho R.N..- Vacancy clustering effect on the electronic and transport properties of bilayer graphene nanoribbons
Nanotechnology - ISSN 1361-6528 - 34:5(2023), 055706
Full text (Publisher's DOI): https://doi.org/10.1088/1361-6528/AC9F50
To cite this reference: https://hdl.handle.net/10067/1920300151162165141

Vacancy clustering effect on the electronic and transport properties of bilayer graphene nanoribbons

L. P. Miranda,[1,*] D. R. da Costa,[1,2,†] F. M. Peeters,[3,‡] and R. N. Costa Filho[1,§]

[1] *Departamento de Física, Universidade Federal do Ceará, Campus do Pici, Fortaleza, Ceará, Brazil*
[2] *Key Laboratory for Micro/Nano Optoelectronic Devices of Ministry of Education & Hunan Provincial Key Laboratory of Low-Dimensional Structural Physics and Devices, School of Physics and Electronics, Hunan University, Changsha 410082, China*
[3] *Department of Physics, University of Antwerp, Groenenborgerlaan 171, B-2020 Antwerp, Belgium*

(Dated: April 28, 2022)

Experimental realizations of two-dimensional materials are hardly free of structural defects such as e.g. vacancies, which, in turn, modify drastically its pristine physical defect-free properties. In this work, we explore effects due to point defect clustering on the electronic and transport properties of bilayer graphene nanoribbons, for AA and AB stacking and zigzag and armchair boundaries, by means of the tight-binding approach and scattering matrix formalism. Evident vacancy concentration signatures exhibiting a maximum amplitude and an universality regardless of the system size, stacking and boundary types, in the density of states around the zero-energy level are observed. Our results are explained via the coalescence analysis of the strong sizeable vacancy clustering effect in the system and the breaking of the inversion symmetry at high vacancy densities, demonstrating a similar density of states for two equivalent degrees of concentration disorder, below and above the maximum value.

I. INTRODUCTION

Bilayer graphene[1–3] (BLG), two coupled monolayers of graphite, has attracted along the last two decades a lot of attention in the field of low-dimensional science and nanotechnology, mostly due to the fact that it shares many of the advantages of graphene's unique properties, such as high electrical mobility[4], as well others not so desired for standard logic applications, as for example, a minimum conductivity at the neutrality point of the order of the conductance quantum[5,6]. In contrast to monolayer graphene (MLG), BLG has an electric field tunable band gap[2,7–10], which can be induced by electrostatic gating, chemical doping or some other parameter, e.g. relying on the electron-electron interaction[2], being of paramount importance for producing high on-off current ratios[11]. This additional electronic feature makes BLG a promising material for applications in optoelectronics and sensors, as for instance to be used to design the next-generation of field effect transistors[12–16] and electrostatic defined BLG quantum dots based devices[17,18].

Although being unwanted, the presence of defects and impurities in experimental realizations of two-dimensional materials are, in general, almost impossible to be avoided and they alter the electronic and transport properties of these systems,[19] by reducing the electronic mobility[20,21] and changing its electronic band structure[22]. Structural defects that modified the crystallographic lattice quality by means of distortion[23,24], reconstruction, displacement are characterized in different manners, such as in-plane defects, that are symmetry-breaking and can include point defects, as for example vacancies[25–32], substitutional impurities, interstitial impurities[29], and interplanar defects, as for instance stacking faults within interlayer stackings[21,33,34].

Due to vacancy disorder in graphene, states localized around missing carbon atoms emerge, being energetically placed around the Fermi level.[25–32,35] The study of vacancies in BLG started even before the first graphene synthesis as reported in Refs. [36,37], and has grown in the last years.[26,28,30,30,33,34,38–41] Therefore, it is of great interest to understand how the electronic transport properties are modified in BLG systems with different kind of boundaries and stacking as a function of the vacancy concentration, in order to determine if their presence is desirable or not.

In this paper, the transition from a BLG to a MLG nanoribbon is studied by analysing the presence of zero modes in the density of states due to point defects. To mimic the lack of control in the position of vacancies, one focuses here on the effects of randomly distributed vacancies in the electronic structure of BLG nanoribbons with armchair and zigzag orientations, which allows the formation of vacancy clustering. The number of states at $E = 0$ eV grows with the number of vacancies and we show that by removing atoms from only one of the layers there is a maximum density of states at $E = 0$ eV followed by a decrease on its value until the MLG behaviour is recovered. A related result was studied by Lucchese, et al.[42] where a competing mechanism between an "activated" and "structurally-disorder" regions was used to explain the evolution of the ratio I_D/I_G (the intensity ratio between the disorder-induced D band and the Raman-allowed first-order G band[43]) with the density of structural defects provoked by low energy (90 eV) Ar^+ ion bombardment. A similar approach will be used here to analyze our system, but instead of using an "activated" region definition the coalescence between the defects will be studied by the clustering of neighbours vacancies. Both AA and AB BLG stacks will be investigated for nanoribbons with different sizes and edges. Our electronic and transport results for the energy spectrum,

density of states (DoS), resistance, and current density for different vacancy concentration are obtained by using the first nearest neighbour hoppings tight-binding (TB) model, and the latter by using the Landauer–Büttiker formalism.

The paper is organized as follows: In Sec. II A the TB model used for the AA and AB BLG are presented, as well as the corresponding band structures for zigzag and armchair BLG nanoribbons. The theoretical framework to define the vacancies and its lattice distribution are explained in Sec. II B. In Sec. III, we discuss the main results for the DoS and the vacancy clustering, and in Sec. IV the transport results. Finally, we summarize our main findings in Sec. V.

II. THEORETICAL MODEL

A. Tight-binding model for BLG

BLG is formed by two MLG stacked over each other[1–3]. Its unit cell is composed by four sublattices, labeled as A_1 and B_1 for layer 1 and A_2 and B_2 for layer 2. The two most common stacks investigated in the literature[1,2,10] are the AB-stacking (named also as Bernal stacking), where atoms in the A_1 sublattice in the bottom layer are linked with B_2 atoms in the top layer, forming a dimer[10], and the AA-stacking, where the atoms in the upper and lower layers are located directly on top of each other. Their crystal structures are sketched in Figs. 1(a) for the AA-stack and 1(b) for the AB-stack. We included only the most significant interlayer hopping term, which is the perpendicular one between the dimer sublattices, γ_1. The other interlayer hopping parameters γ_3 and γ_4 describe interlayer skew couplings between nondimer atoms A_2 and B_1, and between dimer and nondimer atoms A_1 and A_2 or B_1 and B_2, respectively. They are related to the trigonal warping effect leading to an anisotropic band and the electron-hole band asymmetry, respectively, which is out of the main scope of our discussions since the most significant physics investigated here is happening around the Fermi energy and is associated with the zero-modes induced by the vacancies.

The electronic properties of charge carriers in BLG is described here by employing the TB approach within the nearest-neighbor approximation. The TB Hamiltonian for BLG nanoribbons reads explicitly for AB and AA stacking respectively as

$$H_{AB} = H_M - \gamma_1^{AB} \sum_i (a^\dagger_{1,i} b_{2,i} + h.c.), \tag{1a}$$

$$H_{AA} = H_M - \gamma_1^{AA} \sum_{i,j} (a^\dagger_{1,i} a_{2,i} + b^\dagger_{1,j} b_{2,j} + h.c.), \tag{1b}$$

where

$$H_M = -\gamma_0 \sum_{m,i\neq j} (a^\dagger_{m,i} b_{m,j} + h.c.), \tag{1c}$$

where $a^\dagger_{m,i}$ ($a_{m,i}$) creates (annihilates) an electron in site i of sublattice A_m and the operators $b^\dagger_{m,j}$ ($b_{m,j}$) act on the sublattice B_m with $m = 1, 2$ being the layer index. $\gamma_0 = 3.16$ eV is the intralayer hopping between nearest neighbour $A_m - B_m$ sublattices, and $\gamma_1^{AB} = 2\gamma_1^{AA} \approx 0.38$ eV is the interlayer hopping value in AB and AA BLG stack type. We assume that the on-site energy is null, resulting in an electron–hole symmetry for the nanoribbons energy spectra, i.e., it is symmetric with respect to zero energy[10,44]. All calculations discussed here the electron-electron interaction has been neglected. Recent experimental measurements of the confinement properties in BLG-based nanostructures by using scanning tunneling microscope[17,45–49] have been confirmed by single-particle tight-binding calculations, even in the presence of charge defects, impurities, dopants and adatoms[46,48,49], showing that the theoretical framework used here is valid within certain regimes and allows us to have physical insights in the disorder effects on the electronic and transport properties of BLG nanostructures.

For our numerical calculation, we use KWANT[50], an open source Python package for numerical simulation of TB systems with emphasis on quantum transport. It has builtin functions to easily calculate system's transport electronic properties such as band structure, DoS, conductivity, and probability current density. It is able to solve the scattering problem based on a matching wavefunction approach[51] to calculate the transmission of a n-propagating mode in a contact terminal to a m-th mode in another contact. This formulation is mathematically equivalent to the non-equilibrium Green's function with the advantage to be numerically more stable[50]. The differential conductance $G_{sd} = dI_s/dV_d$ between two terminals s and d is calculated by taking the ratio of the differential current of the s-terminal over the differential voltage of the d-terminal, that using the Landauer for-

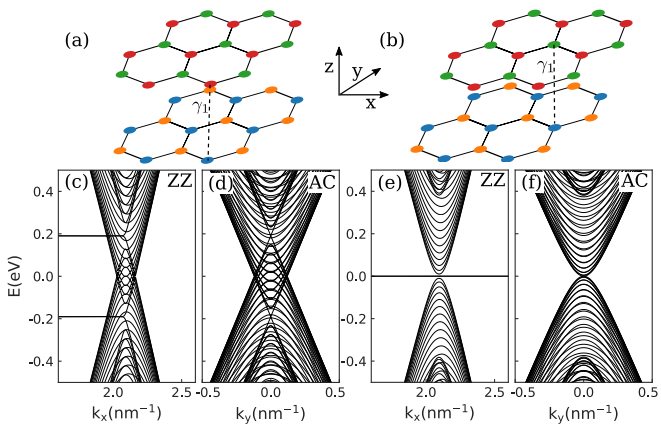

FIG. 1: Lattice structure of (a) AA-stacking BLG and (b) AB-stacking BLG. (c-f) Band structures of BLG nanoribbons for ribbon width of 50 nm and different stacking and edges: (c, d) AA-stack, (e, f) AB-stack, (c, e) zigzag, and (d, f) armchair.

malism reads[50,52]:

$$G_{sd} = \frac{e^2}{h} \sum_{n\in s, m\in d} |S_{nm}|^2, \quad (2)$$

where s and d represent the two electrodes (terminals), standing for source and drain, respectively, and S_{nm} is the scattering matrix. Easily one can obtain the resistance by the inverse of the conductance G.[53] To calculate the DoS, KWANT makes use of the Kernel Polynomial Method[54] which is an efficient way to calculate spectral quantities of large systems in condensed matter physics. With the energy spectrum in hand, the evaluation of the density of states (DoS) is then performed. In principle, DoS describes the proportion of states that are to be occupied by the system at each energy, i.e. a histogram that counts the number of individual energy states in a determined energy range. Its usual numerical calculation is simply done by performing a superposition of individual energy states which one broadens using a Gaussian function $f(E) = \exp\left[-(E-E_0)^2/\Gamma^2\right]$, with a broadening factor usually chosen smaller than the energy levels separations. A broadening factor of $\Gamma = 0.01$ eV is assumed in all figures from here onwards, unless otherwise stated, that is apropriate with the energy separation of the low-energy states of the investigated BLG nanoribbons.

Before investigating the consequences of randomly localized point defects and its clustering on the electronic and transport properties of BLG nanoribbons, it is important to present the defect-free energy spectra for all studied BLG nanoribbon configurations. Figures 1(c)-1(f) show the band structures for the AA [Figs. 1(c, d)] and AB [Figs. 1(e, f)] stacked BLG nanoribbons with ribbon width $W = 50$ nm. Two different nanoribbon boundary terminations are considered: zigzag edge [Figs. 1(c, e)], and armchair edge [Figs. 1(d, f)]. It is well-known in the literature[24,55–66] that armchair MLG nanoribbons present a width-dependent physics, exhibiting either metallic or semiconducting behavior depending on its width, whereas zigzag MLG nanoribbons exhibit a metallic behavior with non-dispersive states in the middle gap, corresponding to surface states strongly localized near the edges. Such general features of edge state physics for zigzag nanoribbons and width-dependent physics for armchair nanoribbons hold true for AB-stacked BLG nanoribbons, as depicted in Figs. 1(e)-1(f). Note that for the chosen width, the armchair AB-stacked BLG nanoribbon is metallic, such that the lowest parabolic bands touching each other at $E = 0$. On the other hand, the lowest energy states of AA-stacked BLG nanoribbons are composed by linear energy spectra consisting by two Dirac cones shifted by $2\gamma_1^{AA}$ (see Figs. 1(c)-1(d)). In addition, for zigzag AA-stacked BLG nanoribbons, the flat states become split (see Fig. 1(c)), exhibiting energies either above or below the Fermi level by a value of γ_1^{AA}. Unlike the AB-stacked BLG case, both zigzag and armchair AA-stacked BLG nanoribbon are metallic regardless of the number of carbon lines.

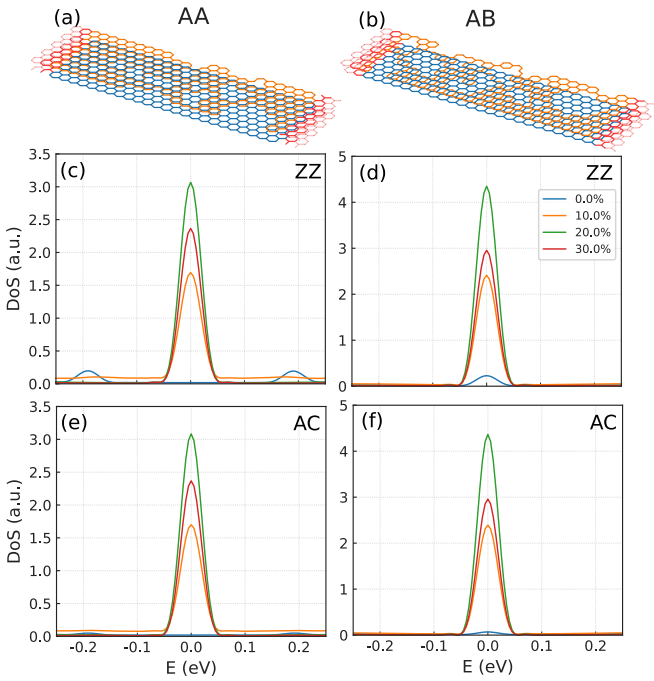

FIG. 2: Schematic illustration of (a) AA- and (b) AB-stacked BLG nanoribbons. Carbon atoms are removed from the top layer (orange). Two ballistic leads (red) are attached to the extremities at the two layers, being used to calculate the conductivity and resistance. (c-f) DoS of the scattering region that defines BLG nanoribbons around the Fermi energy for (left panels) AA- and (right panels) AB-stacked BLG nanoribbons for pristine (blue curve) and defective systems are presented for (c, d) zigzag and (e, f) armchair nanoribbons. Different vacancy densities are taken: 10% (yellow curve), 20% (green curve), and 30% (red curve).

B. Defects in BLG

In TB model, vacancies are implemented by removing atom sites and its connections with neighbouring atoms, making hoppings to the vacancy sites forbidden. There are different types of vacancies defects based on the sublattice symmetry and the number of removed neighbors sites[34,67]. They are named single (SV), double, triple, and so on, vacancy disorders accounting for the number of removed carbon atoms. Related to the imbalance of sublattice atoms, either multiples SVs can be removed without any respect to the sublattice type or all of SVs belonging the same sublattice (e.g. from sublattice A (SVA) and from B (SVB)). The presence of a SV breaks the sublattice symmetry, whereas it can be recovered by a double SV composed by one SVA and one SVB, as well as in double vacancy disorder.[26,27,29,31,32,68] Ref. [68] demonstrated an interesting feature related to different behaviors of these two single vacancy distribution types. They reported that randomly vacancy distribution (i.e. only SVA or only SVB disorders), although inducing an approximately equal number of states as SV disorder for low vacancy concentration, creates considerably different re-

sults in the bend resistance. Moreover, the experimental verification of the vacancy type and impurities (dopants or adatom) in BLG system can be achieved by scanning tunnelling microscopy and spectroscopy measurements, as for instance as reported in Refs. [45,46,48,49]. In particular, Refs. [48] and [49] have experimentally shown by using atomic-scale resolution with scanning tunneling microscopy and spectroscopy the consequences of the points defects on BLG spectrum with a real space characterization.

Here, we focus only on ordinary SVs, being created by randomly removing a single site from one of the layers of the system, regardless its sublattice. In the case of MLG, this randomly carbon atoms removal should preserve the sublattice symmetry on average.[68] The investigated defective BLG nanoribbons are here characterized by the vacancy concentration N with respect to the total number of carbon atoms in the scattering region. The higher the value of N, the larger vacancy clusters can be formed and more edge defects are expected, leading to imperfect edges formed by not just one type of edge, but rather a mix of zigzag and armchair ones. An additional degree of freedom in creating vacancies in bilayer systems is associated with the location of the defect per layer, with the possibility to be created in only one of the layers or in both layers.[26,28,30,30,33,34,38–41] In order to investigate the coalescence due to the transition between BLG and MLG nanoribbons by increasing the vacancy concentration, the electronic and transport properties are studied here by considering multiple randomly distributed SV implemented only on the top-layer, as sketched in Figs. 2(a) and 2(b) for AA-stacked and AB-stacked disordered zigzag BLG nanoribbons, respectively. The sublattice symmetry and inversion symmetry aspects in the investigated BLG nanoribbons shall be very important in understanding the transport results further on here (see discussion in Sec. IV). The examples in Figs. 2(a) and 2(b) have a vacancy concentration of $N = 10\%$. It is important to highlight that the system considered is formed by a scattering (finite system) region that defines the BLG nanoribbon with sample dimension $L \times W$, and consequently small peaks in the DoS associated with the energy states beyond $E = 0$ are not present and, in addition, are not relevant for the electronic aspects investigated here around the Fermi energy. This finite region is generated using KWANT's subroutines[50] by populating a rectangular shaped region (for a specific size) following the BLG unit cell and then the vacancies in a certain concentration are randomly created. However, for a distance $d_r = a_x = 0.24595$ nm (with a_x being the unit cell size in the x-direction) close to the leads, the atoms are not removed. This restriction is set so it will be possible to attach the leads for the transmission calculation. Moreover, the scattering region that defines the BLG nanoribbon is characterized by its width W and then we assumed its length as $L = 3W$, such that the total disordered area is $A = L \cdot W = 3W^2$. This assumption is chosen in order (i) to systematically investigate different vacancy densities associated with large removal carbon atoms numbers and easily compare the results for the different studied situations (edges and stacking); (ii) to deal with BLG nanoribbons dimensions feasible to be experimentally realized; and (iii) to avoid low conductance (high resistance) values due to geometric aspects, such as the small dimensions of the scattering channel, and also skipping-orbit-like trajectories in the density currents in narrow BLG nanoribbons, which could lead to a misunderstanding of the transport properties regarding the presence of vacancies in the system. It is worth mentioning that changes in L size of the scattering region to a fixed width W do not change the nanoribbon band structure since the length L is along the translation symmetry direction, and consequently, one expects not to affect the transport results for the vacancy-free case within the ballistic transport regime.

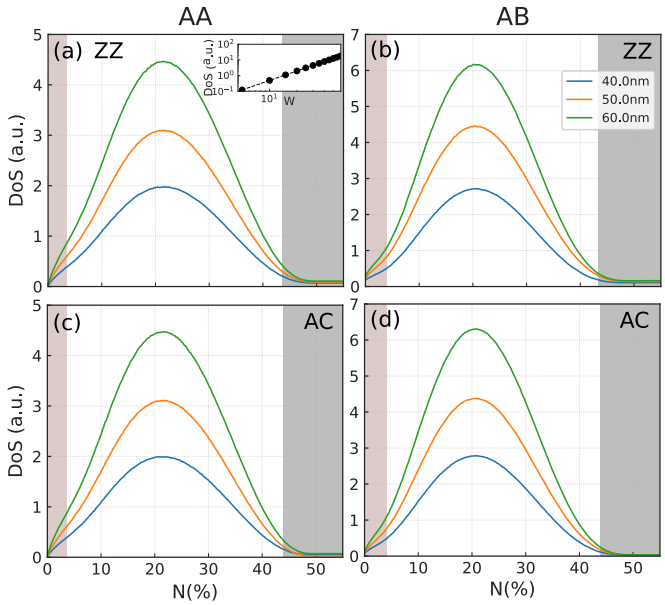

FIG. 3: DoS at $E = 0$ of the scattering region that defines BLG nanoribbons as a function of the vacancies density N for three different ribbon widths (W): (blue) 40 nm, (yellow) 50 nm, and (green) 60 nm, where the ribbon length is defined as $L = 3W$. The total disordered area changes as $A = L \cdot W = 3W^2$. Left (right) panels correspond to AA-(AB-)stacked BLG nanoribbons with (top panels) zigzag and (bottom panels) armchair edges. Each density configuration was averaged by taking twenty samples. It was observed just a small deviation in comparison to the present average curves, that it is caused by the random character of the disordered introduction into the BLG system. For a better visualization of the Gaussian-like DoS profile, we omitted here the error bars. The inset in panel (a) shows a linear fit in log-scale for the centered DoS peak ($\equiv 21\%$) for different zigzag AA-stacked nanoribbon widths W. Its slope is 2.012.

III. ZERO-MODES DENSITY

Let us now investigate the effects of vacancies on the DoS of the scattering region that defines the BLG nanoribbons. Figures 2(c)-2(f) show the DoS for (c, e) AA- and (d, f) AB-stacked BLG nanoribbons with (c, d) zigzag and (e, f) armchair edges. Analyzing the pristine AA-stacked case ($N = 0\%$, blue curve), one finds two peaks around $E = \pm\gamma_1^{AA}$ which are related to the interlayer hoppings, being more pronounced for zigzag case [Fig. 2(c)] due to the degeneracy of the edge states, as shown by the flat states in Fig. 1(c), while for armchair AA-stacked BLG nanoribbons [Fig. 2(e)] they are less evident but non-zero being linked to the corners of the shifted Dirac cones in AA-BLG spectrum. For AB-stacking, one notices a peak at the Fermi energy ($E = 0$), which is related to the edge states present in the zigzag nanoribbon, as depicted by the flat band at $E = 0$ in Fig. 1(e). For armchair BLG nanoribbons with AB-stacking, the presence or the absence of a central peak at $E = 0$ depends on the ribbon width, since it dictates the semiconductor or metallic nature of the ribbon. For the chosen ribbon width, as already discussed for Fig. 1(f), this BLG nanoribbon is metallic, exhibiting, in turn, a less pronounced peak in its DoS [Fig. 2(f)] in comparison to the zigzag case [Fig. 2(d)], that is due to the low degeneracy coming from the conduction-valence band-touching. Results of the DoS at $E = 0$ for semiconductor BLG nanoribbons with armchair edges would present a less pronounced peak but qualitatively similar results to the obtained metallic ones.

The presence of vacancies induces scattering states that are identified by DoS showing a peak at $E = 0$, whose surface area is proportional to the vacancies density[67]. For low vacancy densities, it is expected that zero-modes degeneracy increases and, consequently, the magnitude of the peak at $E = 0$, as observed for $N = 10\%$ (yellow curve) and $N = 20\%$ (green curve) in Figs. 2(c)-2(f). However, for high vacancy concentration the $E = 0$ – DoS peak decreases, as one can see in red curves for $N = 30\%$, where the peak at $E = 0$ for 30% vacancy density is smaller than for 20% for both types of stackings and edges. This behaviour of the DoS at $E = 0$ suggests us the existence of a threshold value for the vacancy concentration, where after this up limit the peak of the DoS decreases. For MLG, most of the studies have been focused on vacancy densities below the percolation threshold ($\lesssim 30\%$)[69].

In order to investigate the universality of the DoS tendency at $E = 0$ for BLG nanoribbons and its link with the coalescence by removing carbon atoms from the top layer of the BLG system into the MLG one, we show in Fig. 3 the DoS value at $E = 0$ varying with the vacancies densities. Results for AA-(AB-)stacked BLG nanoribbons are shown in Figs. 3(a, c) [Figs. 3(b, d)] by taking BLG nanoribbons with different widths and edge types: zigzag (Figs. 3(a, d)) and armchair (Figs. 3(c, d)). Surprisingly, regardless the edge type and the BLG stacking, the evolution of the number of zero-modes in the DoS by increasing the vacancy density for all investigated configurations demonstrates the existence of a saturation point (i.e. an amorphization threshold) observed at $N \approx 21\%$, with a width-independent behavior that resembles a "Gaussian-like" function. To numerically check this result we fit the curves in Fig. 3 with a Gaussian function, defined as $f \equiv DoS(N) = a \exp\left[-(N-b)^2/c\right]$, where a gives insights about the scaling phenomena properties related to

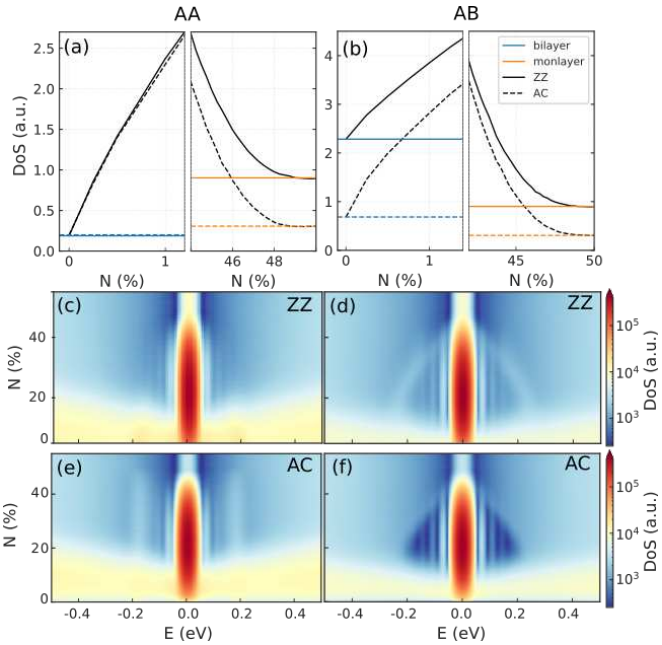

FIG. 4: (a, b) Enlargements of Fig. 3 at low (left) and high (right) vacancy densities for (a) AA-stacked and (b) AB-stacked BLG nanoribbons with ribbon width of 50 nm to emphasize the BLG to MLG transition due to vacancy density increasing. Blue and orange curves are the BLG and MLG DoS values for the pristine cases and the different line types indicate the type of edge orientations. Solid and dashed curves correspond to the pristine DoS values for zigzag and armchair BLG nanoribbons. (c)-(f) Contour plots of the DoS in log scale on the energy-vacancy density plane (E, N) for AA (left panels) and AB (right panels) stacking with nanoribbons formed by (c, d) zigzag and (e, f) armchair edges.

TABLE I: Parameters of the Gaussian-like function fitting, $f \equiv DoS(N) = a \exp\left[-(N-b)^2/c\right]$, for the DoS curves of Fig. 3.

width		AA-ZZ	AA-AC	AB-ZZ	AB-AC
40 nm	a	2.02	2.04	2.75	2.84
	b	21.98	21.9	20.98	21.07
	c	221.3	215.44	189.05	183.58
50 nm	a	3.16	3.18	4.52	4.47
	b	21.94	21.86	20.99	21.10
	c	217.93	212.58	191.78	183.73
60 nm	a	4.56	4.58	6.27	6.44
	b	21.97	21.91	21.06	21.1
	c	217.55	214.47	186.13	183.59

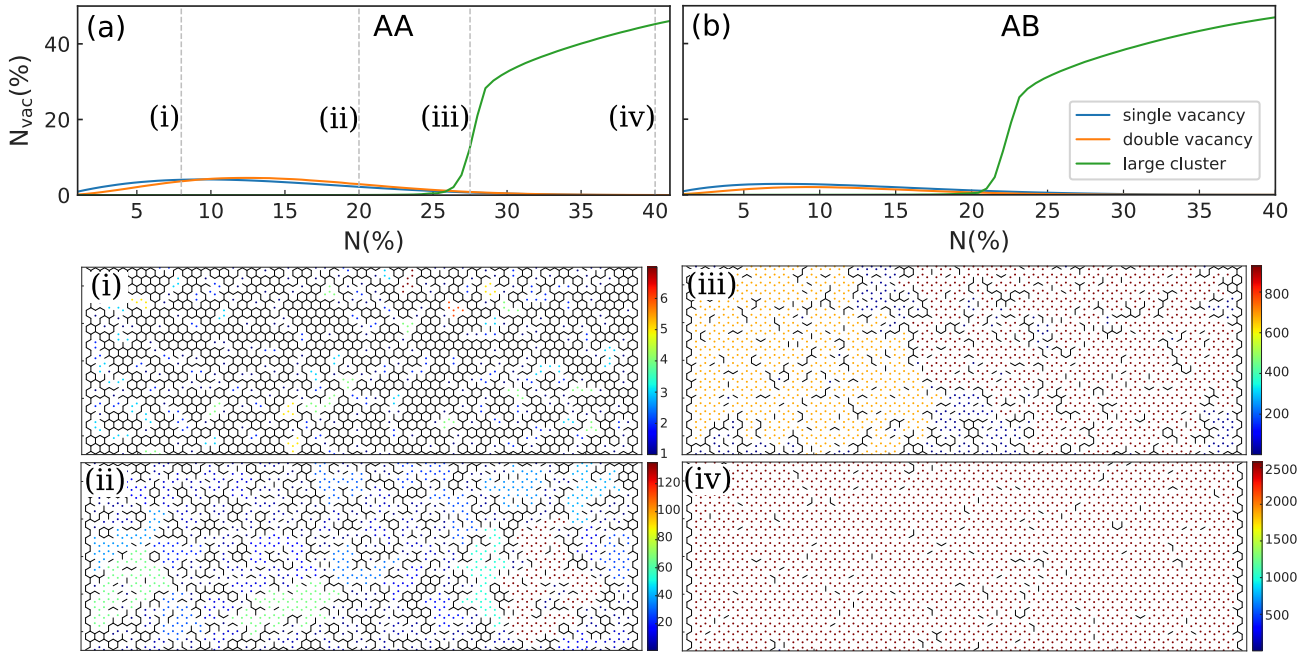

FIG. 5: Vacancy clustering analysis for (a) AA- and (b) AB-stacked BLG nanoribbons with ribbon size 150 nm × 50 nm. Results for single, double, and large clusters of vacancies proportional to the total number of vacancies are shown in blue, yellow, and green. Colored scatter-like plot of the spatial clustering for the systems with vacancies densities at 8%, 20%, 27.5% and 40%, as indicated by the vertical lines in (a), are depicted in the bottom panels (i), (ii), (iii) and (iv), respectively. Each density configuration was averaged by taking five samples.

the Gaussian function amplitude, b is related to Gaussian distribution's mean point, i.e. the center position of the peak, and c is the standard deviation. The fitting parameters are depicted in Table I. Analyzing b–values in Table I, one notes that, in fact, all curves are approximately centered around $\approx 21\%$, and that the a–values show the scalable behavior of the $E = 0$ – DoS with the nanoribbon size, increasing the larger the BLG nanoribbon. This is demonstrated in the inset of Fig. 3(a) with a power-law scaling with a linear fit with slope of ≈ 2.012. After the threshold value $N \approx 21\%$, the DoS for all curves in Fig. 3 decreases until they reach a fixed value corresponding to the DoS of the MLG system. The recovered MLG value is achieved to a vacancy concentration around $\approx 50\%$. This can be seen in Figs. 4(a) and 4(b) where enlargements of Fig. 3 (shaded regions) for low (left panels) and high (right panels) vacancy densities for AA-BLG and AB-BLG, respectively, are shown, emphasizing the transition from pristine BLG nanoribbon to pristine MLG nanoribbon by varying the vacancy density. Dashed and solid curves correspond to armchair and zigzag cases, and blue and orange curves are, respectively, the DoS value for pristine BLG and pristine MLG system.

Owing to verify if such width-, stacking-, and boundary-independent behavior observed in Fig. 3 for the DoS at $E = 0$ holds true for different energies of the investigated BLG nanoribbons, we show in Figs. 4(c)-4(f) contour plots of the DoS in the (E, N)–plane. For a short energy range around $E = 0$, the DoS exhibits a similar behavior as the one discussed for $E = 0$ in Fig. 3 and reaches its higher value (red color) also around $N \approx 21\%$. This is not the case for higher energies that goes to low values (blue color) as N increases, as it should be, since the increase in the number of vacancies mainly affects the degeneracy of the zero-mode states.

To attain a more comprehensive understanding of the Gaussian-like DoS behavior for the electronic states around $E = 0$, we explored the cluster formation and the ratio of single and double vacancies randomly distributed in the top layer of BLG nanoribbons due to the increase of vacancy density N. Without loss of generality, the results for SV (blue curve), double vacancy (yellow curve), and large clusters (green curve) are shown in Fig. 5 just for zigzag AA-stacked (Fig. 5(a)) and AB-stacked (Fig. 5(b)) BLG nanoribbons. We considered that two vacancies belong to the same cluster if they are inside a circle of radius r_c. We choose $r_c = a_x = 0.2459$ nm, which is the unit cell size in the x-direction. Figures 5(a) and 5(b) show that for low vacancy densities (bellow to the observed threshold value, i.e. $N \lessapprox 21\%$) the disordered BLG system is mainly dominated by single and double vacancies. This is confirmed by the spatial clustering analysis depicted in panel (i) for $N = 8\%$ at the bottom of Fig. 5. For higher vacancy densities, the vacancies coalesce and the ratio of single and double vacancies starts to decrease. The formation of the large clusters can be viewed in panel (ii) for $N = 20\%$, in which the spatial clustering analysis exhibits clusters with sizes in the order of ≈ 40 to ≈ 80 removed sites. By increasing even more the dilution on the system's top layer, the N_{vac} percentage of single and

double vacancies tends to zero and a sudden growth of the clusters sizes is observed. Interestingly, this happens approximately around the threshold value found in the DoS plots for energies around $E = 0$. The spatial distributions of the vacancies shown in panels (iii) and (iv) for $N = 27.5\%$ and $N = 40\%$, respectively, confirm this statement. As discussed so far for the AA-BLG case, a similar clustering analysis is observed for disordered AB-stacked BLG nanoribbons, with the difference that the structural transition of the vacancy clustering happens for a slightly smaller vacancy density, as noticed in Fig. 5(b).

It is worth mentioning that a similar analysis of the structural formation of vacancy clusters was performed in Ref. [42], as also mentioned in the Introduction (Sec. I). By Raman Spectroscopy measurements, they showed that the I_D/I_G ratio demonstrated a saturation point where two disorder mechanisms started to compete between themselves. These disorder mechanisms are related with the "activated" and "structurally-disordered" regions. They stated that this competing mechanism is attributed to the coalescence of these two regions and it is followed by a full amorphization or partial sputtering of the graphene layer.

Regarding the skewed interlayer hoppings, it is known that the incorporation of γ_3 leads to the emergence of three-fold mini-valleys around K and K' Dirac cones and consequently to anisotropic low-energy bands for the infinite pristine BLG sheet. Thus, one can easily see that this must lead to an increase in the degeneracy of the DoS at $E = 0$, even in the absence of vacancies, for both the infinite pristine BLG sheet and BLG nanoribbons cases, where in the later one also expects to verify a broadening of the DoS($E = 0$)-peak due to the breaking bands degeneracy, especially for the zigzag BLG nanoribbons where its quasi-flat states become more dispersive by assuming $\gamma_3 \neq 0$.[70] Therefore, the obtained DoS($E = 0$) results discussed here are expected to be qualitatively similar if one takes into account $\gamma_3 \neq 0$, except for an increase in the peak magnitude of DoS($E = 0$).

IV. ELECTRONIC TRANSPORT

In order to have a connection between the DoS behavior and experimental measurements on the electronic transport properties of the system studied here, we calculate the two-terminal resistance, for both the AA and AB-stacked BLG nanoribbons, as function of the vacancy density. The results are shown in Fig. 6 in a semi-log scale with the resistance for energies varying from 0.0 (dark blue color) to 0.2 eV (dark red color). Although the DoS behavior shown in Fig. 3 is basically independent of the stacking and the ribbon orientation, the vacancies affect the transport properties in different ways, depending on the ratio of the number of clusters and their sizes with respect to the system size that can lead to variations on the characteristic transport lengths (e.g. phase relaxation

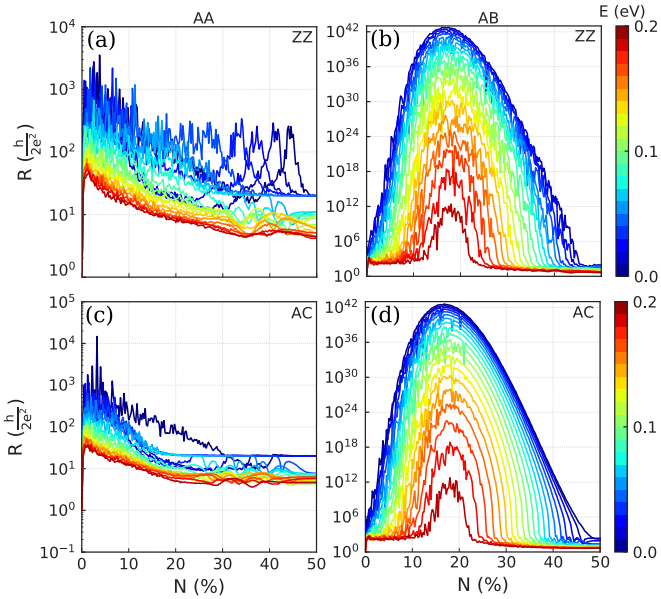

FIG. 6: Resistance as a function of the vacancies density N for (top panels) zigzag and (bottom panels) armchair (left panels) AA-stacked and (right panels) AB-stacked BLG nanoribbons for different Fermi energies. Blue (red) color corresponds to low (high) Fermi energy. Each density configuration was averaged by taking twenty samples.

length and mean free-path) and, consequently, causing transport regimes changes.[53] For the AB stacking (right panels in Fig. 6), there is a rapid increase in the resistance with the number of vacancies, until a maximum is reached (close to N $\approx 17\%$), in an approximately similar way as the observed Gaussian-like DoS profile discussed in previous section. After that, the resistance decreases and reaches a fixed value. By comparing Figs. 6(b) and 6(d) for zigzag and armchair AB-stacked BLG nanoribbons, respectively, one notices a resistance independence on the edge orientation. Previous works reported similar Gaussian-like function characteristics in transport properties of AB-stacked BLG systems.[71,72] For instance, Yu and Duan[72] demonstrated that the on/off current ratio of AB-stacked BLG nanoribbons can be systematically increased upon applying a vertical electric field, which breaks the inversion symmetry, observing a Gaussian-like resistance modulation via applied perpendicular bias. For AA stacking, the results differs a lot from the AB case, even though the DoS are the same. Note that in the disordered investigated system here, we have the following situations: (i) for AA-stacked BLG nanoribbons, where both layers are exactly stacked on top of each other, the presence of a high concentration of randomly distributed multiple SVs in one of the layers does not break the sublattice symmetry on average in that layer[68] and therefore, the inversion symmetry of the system is kept, since the removed interlayer hoppings correspond to the same sublattices on both layers; (ii) for AB-stacked BLG nanoribbons, although the sublattice symmetry is preserved on the disordered top layer, the inversion sym-

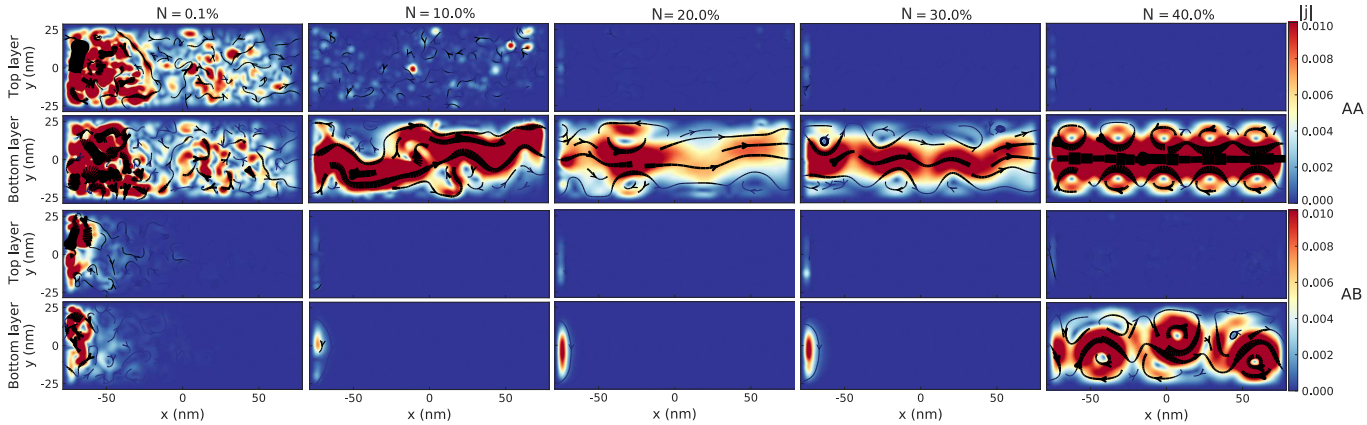

FIG. 7: Current densities for different vacancy concentrations N for zigzag (top panels) AA-stacked and (bottom panels) AB-stacked BLG nanoribbons with ribbon size of 150 nm × 50 nm. Transport modes with energy $E = 0.1$ eV were injected by the left lead and collected in the right lead. Blue (red, black) color corresponds to low (high, very high) densities. Current densities for bottom and top layers are presented separately.

metry is broken in this case, since the removed interlayer connections link sublattices from different types in AB-BLG systems. This is the reason why resistances for both types of stacking and for very low densities ($N < 1\%$) exhibit roughly the same behavior (as will become clear and confirmed later in the discussion for the current densities in first column of Fig. 7), whereas for high vacancy densities the resistance behavior for AA and AB cases is drastically different due to the inversion symmetry to be preserved or broken in the system. Similarly to Ref. [72], the resistance is strongly modulated by the breaking of the inversion symmetry of the AB-stacked BLG system, exhibiting a Gaussian-like profile. In addition, it is worth mentioning that the noised results for the resistance calculated here at $T = 0$ will be smoothed for non-zero temperatures, but one expects that the main features in Fig. 6 remain almost "intact" for non-zero temperatures.

To better understand the resistance results, we analyse in Fig. 7 the current density for the same system setups as in Fig. 6, i.e. zigzag AA-stacked (top panels in Fig. 7) and AB-stacked (bottom panels in Fig. 7) BLG nanoribbons. Different vacancy densities were taken: (first column) 0.1%, (second column) 10%, (third column) 20%, (fourth column) 30%, and (fifth column) 40%. Plots for top and bottom layers are shown separately, in order to identify the origin of the decrease or increase of the resistance in Fig. 6 via insights into the current density amplitudes by increasing the dilution on the system's top layer. The electronic current is injected into the scattering region through the lead on the left side and collected in the lead on the right side. As expected, for low vacancy densities (see first column for $N = 0.1\%$) the current flows in both layers for both AA and AB stacking cases. By increasing the vacancy density on the top layer (analysing the contour plots from left to right columns), the projection of the current on the top layer is suppressed around threshold N–value for AA-stacked BLG case in accordance with the clustering analysis in Fig. 5(a) and with the Gaussian-like DoS profile in Fig. 3(a) for zigzag edge type. One can also notice by the current results for AA stacking that the current in the bottom layer is not strongly affected by changes on the vacancy densities presented in the top layer (see second row of contour plots in Fig. 7). This explains the reason why the resistance in Figs. 6(a) and 6(c) for AA-stacked BLG case remains practically constant for each energy value for vacancy concentration larger than the threshold N–value, disregarding the fluctuations that must be minimized for results with non-zero temperatures. In contrast, for the AB-stacked BLG case with $N > 1\%$, the inversion symmetry broken due to high vacancy densities strongly affects the current, suppressing it in both layers. However, for very high vacancy densities (see fifth column for $N = 40\%$) the current between the two leads is restored for the bottom layer of AB-BLG nanoribbon, resulting in an increase in the conductance and, in turn, a decrease in the resistance, as observed in Figs. 6(b) and 6(d). The absence of current flow in both layers in the AB-stacked BLG case (third and fourth rows of panels in Fig. 7) is in agreement with the large scale of the resistance values, since there are no propagating modes, the conductance is practically null, leading to huge values for the resistance, as seen in Figs. 6(b) and 6(d), in comparison to the range scale of tens of $k\Omega$ to $M\Omega$ usually observed in experimental measurements in BLG systems for the resistance.[72] Although counter-intuitive, the removal of intralayer and interlayer hoppings due to the vacancies in the upper layer affects the electronic transport of the lower layer. It was demonstrated[73,74] that nanostructures formed by MLG-BLG-MLG interfaces allow the confinement of states in the MLG region and also near the MLG-BLG junction even though the bottom layer of such structures does not present explicit edges the electron can nevertheless be influenced by the upper layer edges due to the interlayer coupling near the MLG-BLG junction. Similarly, one observes in our transport results

here the important role of the existence of interlayer connections, which allows scattering between the layers, and the different stacking to avoid non-zero conductance or to suppress propagating states.

V. CONCLUSIONS

Using the nearest-neighbour TB model, the effects of randomly distributed vacancies and its clustering on the electronic and transport properties of BLG nanoribbons were studied by means of the analysis of the DoS at the charge-neutrality point and the resistance, respectively. The disorder is simulated by subtracting carbon atoms of only one of the layers and clusters formations of point defects are allowed. For low densities of vacancies, the DoS at $E = 0$ eV increases as the number of removed atoms increases, owing the enhancement of the zero energy states degeneracy associated with the states localized around missing carbon atoms. Surprisingly, this peak in the DoS has a threshold that is reached for a vacancy concentration value around $N \approx 21\%$. After this value of concentration, the DoS decreases until it approaches to its MLG value. The universality of this behavior is valid regardless the layer stacking (AA or AB), the ribbon orientation (armchair or zigzag), and the nanoribbon width. This result implies that for $N > 21\%$ the empty spaces left by the vacancies start to coalesce forming larger and larger clusters of vacancies in the specific layer.

Although the DoS behavior is the same regardless the stacking and nanoribbon orientation, the transport characteristic is shown to be quite different depending on the stacking. Defects can change the transport characteristics of the material increasing or reducing its conductivity depending on its concentration. Analyzing the resistances for the two investigated types of edges and stackings, it was observed that both zigzag and armchair AB-stacked BLG nanoribbons exhibit a similar feature found for the DoS with two equivalent concentration disorders giving the same resistance value, showing a direct relation between the effects on the DoS by the vacancies and on the electronic transport. The difference between the AA-BLG and AB-BLG transport results are explained by means of the preservation (breaking) of the inversion symmetry for AA (AB) case at high vacancy density. The results presented here emphasise the richness of the BLG properties when vacancies are introduced into the system.

One expects that the incorporation of the next-nearest-neighbor interlayer hoppings (such as the skewed hopping γ_3) will not qualitatively change the electronic results, in particular the ones associated with low-energy spectrum around $E = 0$, e.g. the DoS($E = 0$) results. On the other hand, the electronic transport in the adjacent layer of the BLG nanoribbons should not be drastically affected by point defects created in the other nanoribbon layer. For instance, the near-zero current densities on the adjacent layer due to vacancies on the other layer, as observed in Fig. 7 for $\gamma_3 = 0$, should exhibit a pronounced current to the case $\gamma_3 \neq 0$ even for higher values of vacancy densities than the $\gamma_3 = 0$ case and, therefore, leading to non-null conductance values. This can be envisaged from the fact that when removing an atomic site that has a first near-interlayer-neighbor, its connection is also removed, and thus interlayer scattering is hindered, whereas in the presence of interlayer hoppings such interlayer scattering is still allowed.

ACKNOWLEDGMENTS

The authors are grateful to the National Counsel of Scientific and Technological Development (CNPq), to the National Council for the Improvement of Higher Education (CAPES) of Brazil and to Flemish Science Foundation (FWO-Vl) for financial support. L.P.M is supported by CAPES grant number 88882.349939/2019-01. R.N.C.F and D.R.C are supported by CNPq grant numbers 312384/2018-1, 310019/2018-4 and 437067/2018-1, respectively.

* Electronic address: lucasmiranda@fisica.ufc.br
† Electronic address: diego_rabelo@fisica.ufc.br
‡ Electronic address: francois.peeters@uantwerpen.be
§ Electronic address: rai@fisica.ufc.br

[1] A. H. Castro Neto, F. Guinea, N. M. R. Peres, K. S. Novoselov, and A. K. Geim, Reviews of Modern Physics **81**, 109 (2009).
[2] E. McCann and M. Koshino, Reports on Progress in Physics **76**, 056503 (2013).
[3] A. V. Rozhkov, A. O. Sboychakov, A. L. Rakhmanov, and F. Nori, Physics Reports **648**, 1 (2016).
[4] S. V. Morozov, K. S. Novoselov, M. I. Katsnelson, F. Schedin, D. C. Elias, J. A. Jaszczak, and A. K. Geim, Physical Review Letters **100**, 016602 (2008).
[5] K. S. Novoselov, E. McCann, S. V. Morozov, V. I. Fal'ko, M. I. Katsnelson, U. Zeitler, D. Jiang, F. Schedin, and A. K. Geim, Nature Physics **2**, 177 (2006).
[6] E. V. Castro, N. M. R. Peres, J. M. B. L. Dos Santos, F. Guinea, and A. H. C. Neto, Journal of Physics: Conference Series **129**, 012002 (2008).
[7] M. T. Allen, J. Martin, and A. Yacoby, Nature Communications **3**, 1 (2012).
[8] Y. Zhang, T.-T. Tang, C. Girit, Z. Hao, M. C. Martin, A. Zettl, M. F. Crommie, Y. R. Shen, and F. Wang, Nature **459**, 820 (2009).
[9] K. F. Mak, C. H. Lui, J. Shan, and T. F. Heinz, Physical Review Letters **102**, 256405 (2009).
[10] E. McCann, Physical Review B **74**, 161403(R) (2006).
[11] F. Xia, D. B. Farmer, Y.-m. Lin, and P. Avouris, Nano Letters **10**, 715 (2010).
[12] J. B. Oostinga, H. B. Heersche, X. Liu, A. F. Morpurgo, and L. M. K. Vandersypen, Nature Materials **7**, 151 (2008).

[13] F. W. Chen, H. Ilatikhameneh, G. Klimeck, R. Rahman, T. Chu, and Z. Chen, in *2015 International Conference on Simulation of Semiconductor Processes and Devices (SISPAD)* (IEEE, 2015), pp. 177–181.
[14] B. N. Szafranek, D. Schall, M. Otto, D. Neumaier, and H. Kurz, Nano Letters **11**, 2640 (2011).
[15] M. Cheli, G. Fiori, and G. Iannaccone, IEEE Transactions on Electron Devices **56**, 2979 (2009).
[16] Y. Ouyang, P. Campbell, and J. Guo, Applied Physics Letters **92**, 063120 (2008).
[17] Z. Ge, F. Joucken, E. Quezada, D. R. Da Costa, J. Davenport, B. Giraldo, T. Taniguchi, K. Watanabe, N. P. Kobayashi, T. Low, et al., Nano Letters **20**, 8682 (2020).
[18] J. M. Pereira, P. Vasilopoulos, and F. M. Peeters, Nano Letters **7**, 946 (2007).
[19] P. T. Araujo, M. Terrones, and M. S. Dresselhaus, Materials Today **15**, 98 (2012).
[20] S. Adam, E. H. Hwang, V. M. Galitski, and S. D. Sarma, Proceedings of the National Academy of Sciences **104**, 18392 (2007).
[21] F. Banhart, J. Kotakoski, and A. V. Krasheninnikov, ACS Nano **5**, 26 (2011).
[22] R. N. Costa Filho, G. A. Farias, and F. M. Peeters, Physical Review B **76**, 193409 (2007).
[23] J. S. Nascimento, D. R. da Costa, M. Zarenia, A. Chaves, and J. M. Pereira Jr, Physical Review B **96**, 115428 (2017).
[24] N. S. Bandeira, D. R. da Costa, A. Chaves, G. A. Farias, and R. N. Costa Filho, Journal of Physics: Condensed Matter **33**, 065503 (2020).
[25] J. Kotakoski, A. V. Krasheninnikov, U. Kaiser, and J. C. Meyer, Physical Review Letters **106**, 105505 (2011).
[26] G.-D. Lee, C. Z. Wang, E. Yoon, N.-M. Hwang, D.-Y. Kim, and K. M. Ho, Physical Review Letters **95**, 205501 (2005).
[27] J. J. Palacios, J. Fernández-Rossier, and L. Brey, Physical Review B **77**, 195428 (2008).
[28] K. Kishimoto and S. Okada, Japanese Journal of Applied Physics **55**, 06GF06 (2016).
[29] J. R. Hahn and H. Kang, Physical Review B **60**, 6007 (1999).
[30] H. Xu, T. Heinzel, and I. V. Zozoulenko, Physical Review B **80**, 045308 (2009).
[31] A. A. El-Barbary, R. H. Telling, C. P. Ewels, M. I. Heggie, and P. R. Briddon, Physical Review B **68**, 144107 (2003).
[32] O. Ovdat, Y. Don, and E. Akkermans, Physical Review B **102**, 075109 (2020).
[33] R. H. Telling, C. P. Ewels, A. Ahlam, and M. I. Heggie, Nature Materials **2**, 333 (2003).
[34] A. Vuong, T. Trevethan, C. D. Latham, C. P. Ewels, D. Erbahar, P. R. Briddon, M. J. Rayson, and M. I. Heggie, Journal of Physics: Condensed Matter **29**, 155304 (2017).
[35] Y. C. Chang and S. Haas, Physical Review B **83**, 085406 (2011).
[36] P. A. Thrower and R. M. Mayer, Physica Status Solidi A **47**, 11 (1978).
[37] B. T. Kelly, *Physics of graphite* (Applied Science Publishers, 1981).
[38] K. N. Anindya, M. S. Islam, J. Park, A. G. Bhuiyan, and A. Hashimoto, Current Applied Physics **20**, 572 (2020).
[39] R. E. Mapasha, E. Igumbor, N. F. Andriambelaza, and N. Chetty, Physica B: Condensed Matter **573**, 67 (2019).
[40] E. K. Safari, A. A. Shokri, and M. BabaeiPour, Journal of Magnetism and Magnetic Materials **441**, 230 (2017).
[41] J. J. Palacios and F. Ynduráin, Physical Review B **85**, 245443 (2012).
[42] M. Lucchese, F. Stavale, E. M. Ferreira, C. Vilani, M. Moutinho, R. B. Capaz, C. Achete, and A. Jorio, Carbon **48**, 1592 (2010).
[43] F. Tuinstra and J. L. Koenig, The Journal of Chemical Physics **53**, 1126 (1970).
[44] A. L. Rakhmanov, A. V. Rozhkov, A. O. Sboychakov, and F. Nori, Physical Review Letters **109**, 206801 (2012).
[45] V. Kaladzhyan, S. Pinon, F. Joucken, Z. Ge, E. A. Quezada-Lopez, T. Taniguchi, K. Watanabe, J. Velasco Jr, and C. Bena, Physical Review B **104**, 155418 (2021).
[46] V. Kaladzhyan, F. Joucken, Z. Ge, E. A. Quezada-Lopez, T. Taniguchi, K. Watanabe, J. Velasco Jr, and C. Bena, Physical Review B **104**, 235425 (2021).
[47] Z. Ge, D. Wong, J. Lee, F. Joucken, E. A. Quezada-Lopez, S. Kahn, H.-Z. Tsai, T. Taniguchi, K. Watanabe, F. Wang, et al., Nano Letters **21**, 8993 (2021).
[48] F. Joucken, C. Bena, Z. Ge, E. A. Quezada-Lopez, F. Ducastelle, T. Tanagushi, K. Watanabe, and J. Velasco Jr, Physical Review Letters **127**, 106401 (2021).
[49] F. Joucken, C. Bena, Z. Ge, E. Quezada-Lopez, S. Pinon, V. Kaladzhyan, T. Taniguchi, K. Watanabe, A. Ferreira, and J. Velasco Jr, Nano Letters **21**, 7100 (2021).
[50] C. W. Groth, M. Wimmer, A. R. Akhmerov, and X. Waintal, New Journal of Physics **16**, 063065 (2014).
[51] M. Zwierzycki, P. Khomyakov, A. A. Starikov, K. Xia, M. Talanana, P. X. Xu, V. Karpan, I. Marushchenko, I. Turek, E. W. Bauer, et al., Physica Status Solidi B **245**, 623 (2008).
[52] Y. Imry and R. Landauer, Reviews of Modern Physics **71**, S306 (1999).
[53] S. Datta, *Electronic transport in mesoscopic systems* (Cambridge university press, 1997).
[54] A. Weisse, G. Wellein, A. Alvermann, and H. Fehske, Reviews of Modern Physics **78**, 275 (2006).
[55] L. Brey and H. A. Fertig, Physical Review B **73**, 235411 (2006).
[56] K. Wakabayashi, Y. Takane, M. Yamamoto, and M. Sigrist, New Journal of Physics **11**, 095016 (2009).
[57] K. Wakabayashi, K.-I. Sasaki, T. Nakanishi, and T. Enoki, Science and Technology of Advanced Materials **11**, 054504 (2010).
[58] A. Rozhkov, G. Giavaras, Y. P. Bliokh, V. Freilikher, and F. Nori, Physics Reports **503**, 77 (2011).
[59] C. Stampfer, S. Fringes, J. Güttinger, F. Molitor, C. Volk, B. Terrés, J. Dauber, S. Engels, S. Schnez, A. Jacobsen, et al., Frontiers of Physics **6**, 271 (2011).
[60] N. O. Weiss, H. Zhou, L. Liao, Y. Liu, S. Jiang, Y. Huang, and X. Duan, Advanced Materials **24**, 5782 (2012).
[61] M. Yagmurcukardes, F. M. Peeters, R. T. Senger, and H. Sahin, Applied Physics Reviews **3**, 041302 (2016).
[62] S. Dutta and S. K. Pati, Journal of Materials Chemistry **20**, 8207 (2010).
[63] Y.-W. Son, M. L. Cohen, and S. G. Louie, Physical Review Letters **97**, 216803 (2006).
[64] L. Yang, C.-H. Park, Y.-W. Son, M. L. Cohen, and S. G. Louie, Physical Review Letters **99**, 186801 (2007).
[65] A. V. Rozhkov, S. Savel'ev, and F. Nori, Physical Review B **79**, 125420 (2009).
[66] Y.-W. Son, M. L. Cohen, and S. G. Louie, Nature **444**, 347 (2006).
[67] V. M. Pereira, J. M. B. Lopes dos Santos, and A. H. Castro Neto, Physical Review B **77**, 115109 (2008).
[68] M. D. Petrović and F. M. Peeters, Physical Review B **94**, 235413 (2016).

[69] V. Häfner, J. Schindler, N. Weik, T. Mayer, S. Balakrishnan, R. Narayanan, S. Bera, and F. Evers, Physical Review Letters **113**, 186802 (2014).
[70] A. Knothe and V. Fal'ko, Physical Review B **98**, 155435 (2018).
[71] S. Rathi, I. Lee, M. Kang, D. Lim, Y. Lee, S. Yamacli, H.-I. Joh, S. Kim, S.-W. Kim, S. J. Yun, et al., Scientific Reports **8**, 1 (2018).
[72] W. J. Yu and X. Duan, Scientific Reports **3**, 1 (2013).
[73] D. R. da Costa, M. Zarenia, A. Chaves, J. M. Pereira Jr, G. A. Farias, and F. M. Peeters, Physical Review B **94**, 035415 (2016).
[74] M. Mirzakhani, M. Zarenia, S. A. Ketabi, D. R. da Costa, and F. M. Peeters, Physical Review B **93**, 165410 (2016).